Progress In Electromagnetics Research, Vol. 106, 225–241, 2010

NON-ITERATIVE IMAGING OF THIN ELECTROMAGNETIC INCLUSIONS FROM MULTI-FREQUENCY RESPONSE MATRIX

W. K. Park

Department of Mathematics
Kookmin University
Seoul, 136-702, Korea

Abstract—Although MUSIC (MUltiple SIgnal Classification)-type algorithm has shown feasibilities as a non-iterative imaging technique of thin penetrable electromagnetic inclusion from its far-field multi-static response (MSR) matrix, it induces a poor result whenever one tries to obtain such inclusion of both dielectric and magnetic contrast with respect to the embedding homogeneous space $\mathbb{R}^2$ case. In this paper, we develop an improved non-iterative imaging algorithm based on the modeling of multi-frequency MSR matrix according to a rigorous asymptotic expansion of the scattering amplitude. Numerical examples exhibit that presented algorithm performs satisfactorily for single and multiple thin inclusions, even with a fair amount of random noise.

1. INTRODUCTION

Recent progress towards inverse problem is highly remarkable due to the developments of the computing system environment. One of the many interests in inverse problem is the non-destructive evaluation of electromagnetic inhomogeneities embedded in known media using high/low frequency time-harmonic electromagnetic propagation arising in physics, medical science, material engineering, etc. Related works can be found in [1–5, 8, 10–15, 20, 21, 23, 27–30] and the references therein. Throughout the literature, various algorithms for reconstructing an unknown object have been suggested, most being based on Newton-type iteration schemes. Yet, for successful application, one needs a good initial guess, close enough

Received 25 May 2010, Accepted 13 July 2010, Scheduled 25 July 2010
Corresponding author: W. K. Park (parkwk@kookmin.ac.kr).

to the unknown object. Without it, one might suffer from large computational costs with the risk of non-convergence also. Moreover, iterative schemes require not only suitable regularization terms depending upon the specific problem at hand but also complex calculation of Fréchet derivatives at each iteration step.

In order to overcome such difficulties, alternative non-iterative imaging algorithm has been suggested. Among them, MUSIC (MUltiple SIgnal Classification)-type algorithm is successfully applied to the imaging of penetrable, electromagnetically thin inclusions as well as one of the perfectly conducting ones at a fixed single frequency. From the results in [24, 25], it has been shown that this algorithm is fast, effective and robust. However, in the imaging of thin inclusion of both dielectric and magnetic contrast with respect to the embedding homogeneous space $\mathbb{R}^2$ case, one obtains a poor result so that an improvement is required. Recently, an effective and robust multi-frequency algorithm has been proposed so as to find the location of small perfectly conducting cracks [3] and dielectric thin inclusions within a homogeneous half-space [23], but a suitable algorithm for extended inclusions of both dielectric and magnetic contrast is still expected.

The purpose of this paper is to develop a non-iterative imaging algorithm which is effective to retrieve electromagnetically thin penetrable inclusions of dielectric and magnetic contrast with respect to the embedding homogeneous space $\mathbb{R}^2$. It is based on the fact that the Multi-Static Response (MSR) matrix can be modeled via a rigorously derived asymptotic expansion formula of the scattering amplitude in the presence of such inclusions. A number of numerical simulations will then illustrate how the proposed imaging algorithm operated at several frequencies behaves and enhances the imaging performance.

This paper is structured as follows. In Section 2, we briefly discuss the two-dimensional direct scattering problem and introduce the asymptotic expansion formula for the scattering amplitude. In Section 3, non-iterative imaging algorithm is sketched, and corresponding numerical examples are shown in Section 4. Section 5 contains a brief conclusion. A brief discussion of statistical hypothesis testing is given in the appendix.

2. DIRECT SCATTERING PROBLEM

Let us consider two-dimensional electromagnetic scattering from a thin, curve-like homogeneous inclusion within a homogeneous space $\mathbb{R}^2$. The latter contains an inclusion denoted by Γ which is localized in the

neighborhood of a curve σ. That is,

$$\Gamma = \{x + \eta n(x) : x \in \sigma,\ \eta \in (-h, h)\},$$

where the supporting σ is a simple, smooth curve in $\mathbb{R}^2$. $n(x)$ is the unit normal to σ at x, and h is a strictly positive constant which specifies the thickness of the inclusion (small with respect to the wavelength λ).

Constitutive materials are fully characterized by their dielectric permittivity and magnetic permeability at a given frequency. Let $0 < \varepsilon_0 < +\infty$ and $0 < \mu_0 < +\infty$ denote the permittivity and permeability of the embedding space $\mathbb{R}^2$, and $0 < \varepsilon < +\infty$ and $0 < \mu < +\infty$ the ones of the inclusion Γ. Then, the piecewise constant dielectric permittivity and magnetic permeability can be written as

$$\varepsilon(x) = \begin{cases} \varepsilon & \text{for} \quad x \in \Gamma \\ \varepsilon_0 & \text{for} \quad x \in \mathbb{R}^2 \backslash \bar{\Gamma} \end{cases} \quad \text{and} \quad \mu(x) = \begin{cases} \mu & \text{for} \quad x \in \Gamma \\ \mu_0 & \text{for} \quad x \in \mathbb{R}^2 \backslash \bar{\Gamma}, \end{cases}$$

respectively. If there is no inclusion, i.e., in the homogeneous space, $\mu(x)$ and $\varepsilon(x)$ are equal to μ_0 and ε_0 respectively.

At strictly positive operation frequency ω (wavenumber $k_0 = \omega\sqrt{\varepsilon_0 \mu_0}$), let $u(x)$ be the time-harmonic total field which satisfies the Helmholtz equation in the presence of thin inclusion:

$$\nabla \cdot \left(\frac{1}{\mu(x)} \nabla u(x) \right) + \omega^2 \varepsilon(x) u(x) = 0 \quad \text{in} \quad \mathbb{R}^2.$$

Let $u_0(x)$ be the solution to the Helmholtz equation in the absence of such inclusion. Then, as usual, the total field u divides itself into the incident field u_0 and scattered field u_s, $u = u_0 + u_s$. Notice that this unknown scattered field $u_s(x)$ satisfies the Sommerfeld radiation condition

$$\lim_{|x| \to \infty} \sqrt{|x|} \left(\frac{\partial u_s(x)}{\partial |x|} - ik_0 u_s(x) \right) = 0$$

uniformly in all directions $\hat{x} = \frac{x}{|x|}$.

The following expressions are needed to introduce the asymptotic expansion as done next.

Definition 2.1 *For every $x \in \sigma$, let $\tau(x)$ and $n(x)$ be unit vectors that are respectively tangent with and normal to σ at x. The symmetric matrix $\mathcal{A}(x)$ is as such [6, 7]:*

- *$\mathcal{A}(x)$ has eigenvectors $\tau(x)$ and $n(x)$,*
- *The eigenvalue corresponding to $\tau(x)$ is $2\left(\frac{1}{\mu} - \frac{1}{\mu_0}\right)$,*
- *The eigenvalue corresponding to $n(x)$ is $2\left(\frac{1}{\mu_0} - \frac{\mu}{\mu_0^2}\right)$.*

Now, let us specialize u_0 to incident plane waves

$$u_0(x) = e^{ik_0\theta\cdot x} \quad \text{for} \quad x \in \mathbb{R}^2$$

and far fields in free space where $\theta = (\theta_x, \theta_y)$ is a two-dimensional vector on the unit circle S^1 in $\mathbb{R}^2$, i.e., θ satisfies $\theta \cdot \theta = 1$. Let $\{\hat{y}_j\}_{j=1}^N \subset S^1$ be a discrete finite set of observation directions and $\{\theta_l\}_{l=1}^N \subset S^1$ be the same number of incident directions. By combining the results of [5–7], one is able to obtain the following asymptotic expansion: for $y \in \mathbb{R}^2 \backslash \bar{\Gamma}$,

$$u(y) = u_0(y) + u_s(y) = u_0(y) + hu_\sigma(y) + o(h) \tag{1}$$

where the correction term u_σ is given by

$$u_\sigma(y) = \int_\sigma \left[\nabla u_0(x)\cdot\mathcal{A}(x)\cdot\nabla_x G(x,y) + \omega^2(\varepsilon-\varepsilon_0)u_0(x)G(x,y)\right]d\sigma(x)$$

, and

$$G(x,y) = -\frac{i}{4}H_0^1(k_0\,|x-y|)$$

is the two-dimensional time harmonic Green function.

The scattering amplitude is defined as a function $K(\hat{y},\theta)$ which satisfies

$$u_s(y) = \frac{e^{ik_0|y|}}{\sqrt{|y|}}K(\hat{y},\theta) + o\left(\frac{1}{\sqrt{|y|}}\right)$$

as $|y| \longrightarrow \infty$ uniformly on $\hat{y} = y/|y|$ and $\theta \in S^1$. From the asymptotic behavior of G and a simple calculation, one easily derives:

$$\begin{aligned} G(x,y) &= \frac{1+i}{4\sqrt{k_0\pi}}\frac{e^{ik_0|y|}}{\sqrt{|y|}}e^{-ik_0\frac{y}{|y|}\cdot x} + o\left(\frac{1}{\sqrt{|y|}}\right) \\ \nabla_x G(x,y) &= \frac{1+i}{4\sqrt{k_0\pi}}\frac{e^{ik_0|y|}}{\sqrt{|y|}}\left(-ik_0\frac{y}{|y|}\right)e^{-ik_0\frac{y}{|y|}\cdot x} + o\left(\frac{1}{\sqrt{|y|}}\right) \end{aligned} \tag{2}$$

as $|y| \longrightarrow \infty$. By combining (1) and (2), the asymptotic formula for the scattering amplitude follows as

$$K(\hat{y},\theta) = h\frac{k_0^2(1+i)}{4\sqrt{k_0\pi}}\int_\sigma\left(\frac{\varepsilon-\varepsilon_0}{\sqrt{\varepsilon_0\mu_0}} - \hat{y}\cdot\mathcal{A}(x)\cdot\theta\right)e^{ik_0(\theta-\hat{y})\cdot x}d\sigma(x) + o(h), \tag{3}$$

where $o(h)$ is uniform in $x \in \sigma$ and $\hat{y}, \theta \in S^1$.

3. NON-ITERATIVE MULTI-FREQUENCY IMAGING ALGORITHM

In this section, we apply the asymptotic formula for the scattering amplitude (3) so as to build up the imaging algorithm. To do so, we use the eigenvalue structure of the Multi-Static Response (MSR) matrix $\mathcal{K} = (K_{jl})$, whose element K_{jl} is the amplitude collected at observation number j for the incident wave numbered l.

Let us assume that for a given frequency ω, the thin inclusion is divided into M different segments of size of order $\frac{\lambda}{2}$. Having in mind the Rayleigh resolution limit from far-field data, any detail less than one-half of the wavelength cannot be retrieved, and only one point, say x_m for $m = 1, 2, \ldots, M$, at each segment is expected to contribute to the image space of the response matrix $\mathcal{K}$ [2, 18, 24, 25].

For simplicity, let us remove the residue term $o(h)$ from (3). Then, for each $\hat{y}_j = -\theta_j$, the $jl-$th element of the MSR matrix $K_{jl} \in \mathbb{C}$, $j, l = 1, 2, \ldots, N$, is

$$\begin{aligned} K_{jl} &= K(\hat{y}_j, \theta_l)|_{\hat{y}_j = -\theta_j} \\ &= h\frac{k_0^2(1+i)}{4\sqrt{k_0\pi}} \int_\sigma \left(\frac{\varepsilon - \varepsilon_0}{\sqrt{\varepsilon_0\mu_0}} + \theta_j \cdot \mathcal{A}(x) \cdot \theta_l \right) e^{ik_0(\theta_j+\theta_l)\cdot x} d\sigma(x) \\ &\approx h\frac{k_0^2(1+i)}{4\sqrt{k_0\pi}} \frac{|\sigma|}{M} \sum_{m=1}^{M} \left[\frac{\varepsilon - \varepsilon_0}{\sqrt{\varepsilon_0\mu_0}} + 2\left(\frac{1}{\mu} - \frac{1}{\mu_0}\right) \theta_j \cdot \tau(x_m)\theta_l \cdot \tau(x_m) \right. \\ &\quad \left. + 2\left(\frac{1}{\mu_0} - \frac{\mu}{\mu_0^2}\right) \theta_j \cdot n(x_m)\theta_l \cdot n(x_m) \right] e^{ik_0(\theta_j+\theta_l)\cdot x_m}, \end{aligned}$$

where $|\sigma|$ denotes the length of σ.

Notice that MSR matrix $\mathcal{K}$ can be decomposed as follows:

$$\mathcal{K} = \mathcal{D}\mathcal{E}\mathcal{D}^T. \tag{4}$$

Here, the matrix $\mathcal{E} \in \mathbb{R}^{3M\times 3M}$ is a diagonal matrix with component

$$\mathcal{E} = h\frac{k_0^2(1+i)}{4\sqrt{k_0\pi}} \frac{|\sigma|}{M} \begin{pmatrix} E_\varepsilon & 0 \\ 0 & E_\mu \end{pmatrix},$$

where

$E_\varepsilon = M \times M$ diagonal matrix with components $\dfrac{\varepsilon - \varepsilon_0}{\sqrt{\varepsilon_0\mu_0}}$,

$E_\mu = 2M \times 2M$ diagonal matrix with 2×2 blocks

$$\begin{pmatrix} 2\left(\frac{1}{\mu} - \frac{1}{\mu_0}\right) & 0 \\ 0 & 2\left(\frac{1}{\mu_0} - \frac{\mu}{\mu_0^2}\right) \end{pmatrix}$$

and the matrix $\mathcal{D} \in \mathbb{C}^{N\times 3M}$ can be written as follows

$$\begin{pmatrix} D_\varepsilon^1 & D_\varepsilon^2 & \dots & D_\varepsilon^M & D_\mu^1 & D_\mu^2 & \dots & D_\mu^{2M} \end{pmatrix}$$

where

$$D_\varepsilon^m = \left(e^{ik_0\theta_1\cdot x_m}, e^{ik_0\theta_2\cdot x_m}, \dots, e^{ik_0\theta_N\cdot x_m} \right)^T,$$

$$D_\mu^{2(m-1)+s} = \left(\theta_1 \cdot \xi_s(x_m) e^{ik_0\theta_1\cdot x_m}, \dots, \theta_N \cdot \xi_s(x_m) e^{ik_0\theta_N\cdot x_m} \right)^T$$

with

$$\xi_s(x_m) := \begin{cases} \tau(x_m) & \text{if} \quad s = 1 \\ n(x_m) & \text{if} \quad s = 2. \end{cases}$$

Let us notice that with the representation (4), $\mathcal{K}$ is symmetric but not Hermitian (a Hermitian matrix could be formed as $\mathcal{K}\bar{\mathcal{K}}$). Since $\mathcal{K}$ is not self-adjoint, a Singular Value Decomposition (SVD) has to be used instead of the eigenvalue decomposition [9]. Let us perform this decomposition of matrix $\mathcal{K}$, and let M be the number of nonzero singular values for the given ω. Then, $\mathcal{K}$ can be represented as follows:

$$\mathcal{K} = \mathcal{U}(\omega)\mathcal{S}(\omega)\bar{\mathcal{V}}^T(\omega) \approx \sum_{m=1}^{M} u_m(\omega) s_m(\omega) \bar{v}_m^T(\omega),$$

where $s_m(\omega)$ are the singular values. $u_m(\omega)$ and $v_m(\omega)$ are the left and right singular vectors of $\mathcal{K}$ for $m = 1, 2, \dots, M$.

Based on the above singular value decomposition, the imaging algorithm is developed as follows. For $c \in \mathbb{R}^3 \setminus \{0\}$, let us define a vector

$$d(x;\omega) = \left(c\cdot(1,\theta_1) e^{ik_0\theta_1\cdot x}, c\cdot(1,\theta_2) e^{ik_0\theta_2\cdot x}, \dots, c\cdot(1,\theta_N) e^{ik_0\theta_N\cdot x} \right)^T \tag{5}$$

and corresponding normalized vector $\hat{d}(x;\omega) = \frac{d(x;\omega)}{||d(x;\omega)||}$. Then

$$u_m(\omega) \sim e^{i\gamma_m^1} \hat{d}(x_m;\omega) \quad \text{and} \quad \bar{v}_m(\omega) \sim e^{i\gamma_m^2} \hat{d}(x_m;\omega) \tag{6}$$

for some γ_m^1 and γ_m^2, $m = 1, 2, \dots, M$ [3, 17]. Since the first M columns of the matrix $\mathcal{U}(\omega)$ and $\mathcal{V}(\omega)$, $\{u_1(\omega), u_2(\omega), \dots, u_M(\omega)\}$ and $\{v_1(\omega), v_2(\omega), \dots, v_M(\omega)\}$, are orthonormal, one can easily find that

$$\begin{aligned} &\langle \hat{d}(x;\omega), u_m(\omega)\rangle \neq 0 \quad \text{and} \quad \langle \hat{d}(x;\omega), \bar{v}_m(\omega)\rangle \neq 0 \quad \text{if} \quad x = x_m \\ &\langle \hat{d}(x;\omega), u_m(\omega)\rangle \approx 0 \quad \text{and} \quad \langle \hat{d}(x;\omega), \bar{v}_m(\omega)\rangle \approx 0 \quad \text{if} \quad x \neq x_m \end{aligned} \tag{7}$$

for $m = 1, 2, \dots, M$, where $\langle a, b\rangle = \bar{a}\cdot b$.

Thus, we can construct an image function at given frequency ω as:

$$\mathrm{W}_S(x) = \sum_{m=1}^{M} |\langle \hat{d}(x;\omega), u_m(\omega)\rangle \langle \hat{d}(x;\omega), \bar{v}_m(\omega)\rangle|. \tag{8}$$

Based on the observation (7), the map of $W_S(x)$ should exhibit peaks of magnitude of 1 at location $x = x_m$ for $m = 1, 2, \ldots, M$, and of small magnitude at $x \in \mathbb{R}^2 \backslash \bar{\Gamma}$.

Unfortunately, image function (8) at single frequency offers an image with poor resolution [3, 23] (also see Figure 4). In order to improve the imaging performance, we suggest a normalized image function at several frequencies $\{\omega_f : f = 1, 2, \ldots, F\}$ as

$$\mathrm{W}(x) = \frac{1}{F} \sum_{f=1}^{F} \sum_{m=1}^{M_f} |\langle \hat{d}(x;\omega_f), u_m(\omega_f)\rangle \langle \hat{d}(x;\omega_f), \bar{v}_m(\omega_f)\rangle|. \tag{9}$$

where M_f is the number of nonzero singular values of MSR matrix at ω_f for $f = 1, 2, \ldots, F$. Then, similarly with the (8), the map of $\mathrm{W}(x)$ is expected to exhibit peaks of magnitude of 1 at location x_m for $m = 1, 2, \ldots, M_f$ and of small magnitude at $x \in \mathbb{R}^2 \backslash \bar{\Gamma}$. A suitable number of M_f for each frequency ω_f can be found via careful thresholding, see [24, 25] for instance.

It is worth mentioning that (9) is an improved version of an important Kirchhoff migration:

$$\begin{aligned} \mathrm{W}_{\mathrm{KIR}}(x) &= |\langle d(x;\omega), \mathcal{K} d(x;\omega)\rangle| \\ &= \sum_{m=1}^{N} s_m(\omega) |\langle \hat{d}(x;\omega), u_m(\omega)\rangle \langle \hat{d}(x;\omega), \bar{v}_m(\omega)\rangle|. \end{aligned} \tag{10}$$

Formula (9) uses only proper singular vectors corresponding to the supporting curve σ, so it is expected that peaks of magnitude of 1 will be concentrated along the σ, accurately. Moreover, from the fact that the singular values of $\mathcal{K}$ are highly influenced by random noise, imaging via (10) should yield a poor result when the measured data are polluted with it. However, (9) does not contain the singular values, i.e., it will allow a more accurate result in the presence of random noise. Finally, based on the statistical hypothesis testing [3], multiple frequencies should guarantee the imaging performance via higher signal-to-noise ratio (SNR). For reader's convenience, we briefly state it in the appendix. Comparisons of imaging results will be exhibited in the next section (see Figures 3 and 4).

By virtue of [25], we briefly introduce a MUSIC-type image function at a single frequency ω. Let us define a corresponding

projection onto the null (or noise) subspace

$$\mathrm{P}_{\mathrm{noise}}(d(x;\omega)) = \sum_{m>M} u_m(\omega)\bar{u}_m^T(\omega)d(x;\omega).$$

Then an image of x_m, $m = 1, 2, \ldots, M$, follows from computing

$$\mathrm{W}_{\mathrm{MUSIC}}(x) = \frac{1}{||\mathrm{P}_{\mathrm{noise}}(d(x;\omega))||}. \tag{11}$$

The resulting plot of this estimator (11) is expected to exhibit large peaks at the sought x_m.

4. NUMERICAL EXAMPLES

In this section, numerical examples are illustrated for demonstrating the effectiveness of imaging algorithm. For that purpose, two σ_j characteristics of the thin inclusion Γ_j are chosen for illustration:

$$\sigma_1 = \left\{(z - 0.2, -0.5z^2 + 0.4) : z \in [-0.5, 0.5]\right\}$$
$$\sigma_2 = \left\{(z + 0.2, z^3 + z^2 - 0.5) : z \in [-0.5, 0.5]\right\}$$

Throughout this section, let us denote by ε_j and μ_j the permittivities and permeabilities of Γ_j, respectively. The thickness h of the Γ_j is set to 0.015. Parameters ε_0 and μ_0 are chosen as 1. The applied frequency is $\omega_f = \frac{2\pi}{\lambda_f}$; here λ_f, $f = 1, 2, \ldots, 20$, is the given wavelength. In this paper, frequencies ω_f are equi-distributed within the interval $[\omega_1, \omega_{20}]$. As for the illumination and observation directions $\theta_l \in S^1$, they are selected as

$$\theta_l = \left(\cos\frac{2\pi l}{N}, \sin\frac{2\pi l}{N}\right) \quad \text{for} \quad l = 1, 2, \ldots, N.$$

Let us emphasize that the data set of the MSR matrix $\mathcal{K}$ is generated by Finite Element Method (FEM) via a very fine meshes[†]. Then, a white Gaussian noise with 20 dB signal-to-noise ratio (SNR) is added to the unperturbed data in order to show the robustness of the proposed algorithm. For obtaining the number of nonzero singular values M_f at each frequency ω_f, a 0.01-threshold scheme (choosing first j singular values $s_j(\omega_f)$ such that $\frac{s_j(\omega_f)}{s_1(\omega_f)} \geq 0.01$) is adopted. A more detailed discussion of thresholding can be found in [24, 25]. The search domain Ω is defined as $\Omega = [-1, 1] \times [-1, 1]$. As for the step

[†] Alternatively, one can employ an asymptotic formulation involving the solution of a second-kind Fredholm integral equation along the supporting curve [22]. See [25] for corresponding results.

size of the search points $x \in \Omega$, it is taken of the order of 0.04. The vector c of (5) is chosen $c = (1, 0, 1)$ (see [25, Section 4] for a detailed discussion).

Let us consider the imaging of Γ_1. MSR matrix $\mathcal{K}$ is collected for $N = 36$ and frequencies $\omega_f \in [\frac{2\pi}{0.5}, \frac{2\pi}{0.2}]$. Map of $\mathrm{W}(x)$ and $\mathrm{W}_{\mathrm{MUSIC}}(x)$ are displayed in Figure 1. Although $\mathrm{W}_{\mathrm{MUSIC}}(x)$ offers an acceptable but not so good result, the proposed algorithm gives a good result so that one can successfully recognize Γ_1.

In Figure 2, a thin inclusion of complex shape Γ_2 is illustrated. MSR matrix $\mathcal{K}$ is collected for $N = 40$ and frequencies $\omega_f \in [\frac{2\pi}{0.4}, \frac{2\pi}{0.2}]$. Similarly with the previous imaging of Γ_1, the proposed algorithm gives

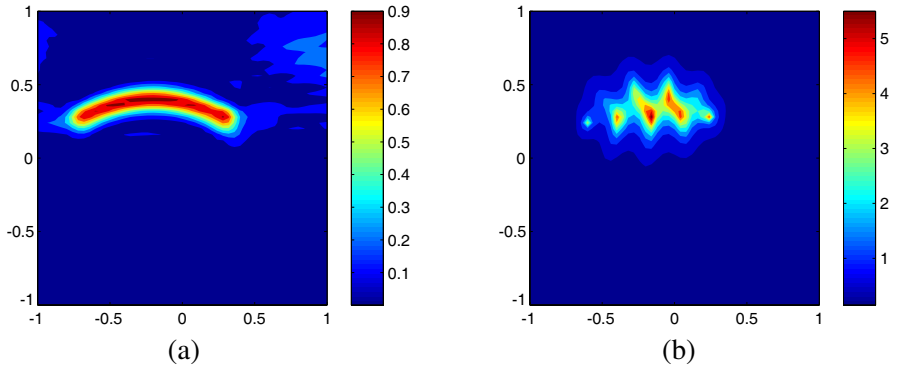

Figure 1. Map of $\mathrm{W}(x)$ and $\mathrm{W}_{\mathrm{MUSIC}}(x)$ for Γ_1. (a) Map of $\mathrm{W}(x)$. (b) Map of $\mathrm{W}_{\mathrm{MUSIC}}(x)$ at $\omega = \frac{2\pi}{0.5}$.

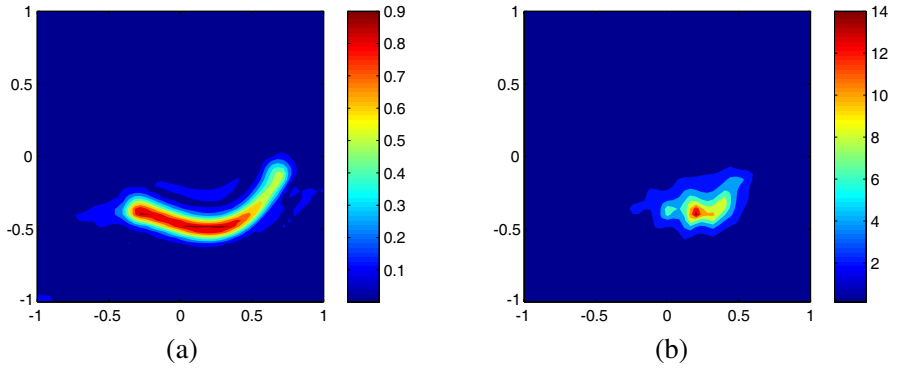

Figure 2. Map of $\mathrm{W}(x)$ and $\mathrm{W}_{\mathrm{MUSIC}}(x)$ for Γ_2. (a) Map of $\mathrm{W}(x)$. (b) Map of $\mathrm{W}_{\mathrm{MUSIC}}(x)$ at $\omega = \frac{2\pi}{0.4}$.

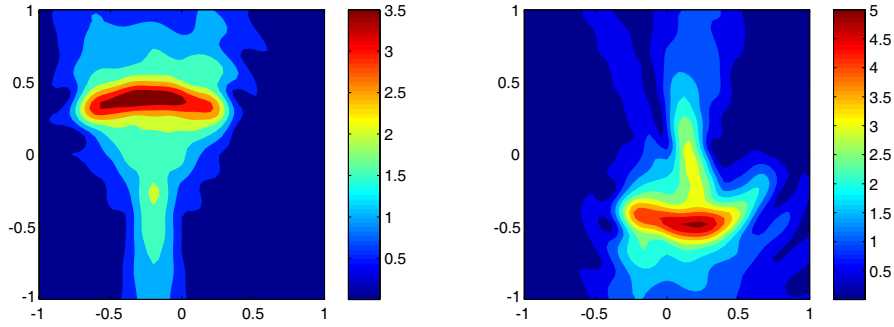

Figure 3. Map of $W_{KIR}(x)$ for Γ_1 and Γ_2. (a) Map of $W_{KIR}(x)$ at $\omega = \frac{2\pi}{0.5}$. (b) Map of $W_{KIR}(x)$ at $\omega = \frac{2\pi}{0.4}$.

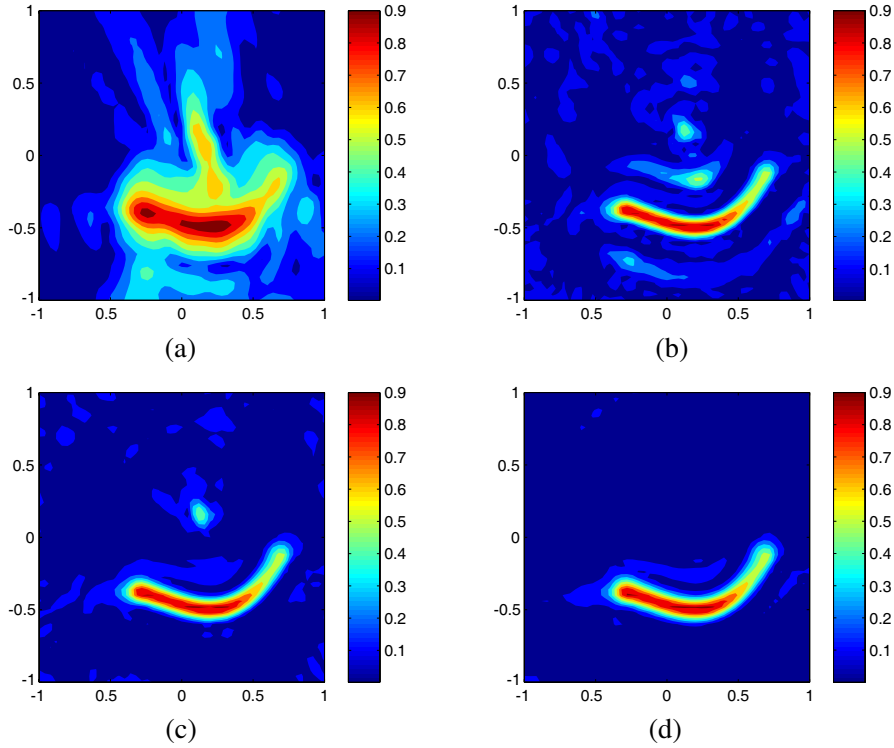

Figure 4. (Influence of applied frequency) Map of $W(x)$ for different number of applied frequencies F when the thin inclusion is Γ_2. (a) Map of $W(x)$ for $F = 1$. (b) Map of $W(x)$ for $F = 3$. (c) Map of $W(x)$ for $F = 5$. (d) Map of $W(x)$ for $F = 10$.

a good result, but a poorer resolution is achieved via $\mathrm{W}_{\mathrm{MUSIC}}(x)$.

Figure 3 shows the imaging result via Kirchhoff migration (10). Although it offers a good result against the MUSIC-type one, it cannot retrieve the shape of such inclusions successfully.

Figure 4 displays the role of number of applied frequencies under the same test configuration of Γ_2. By comparing Figures 4(a)–4(d), one can easily observe that multiple frequencies enhance the imaging performance. There is one point to observe at this stage. Figures 4(b) and 4(c) contain a number of weak replicas and an isolated point of large magnitude, respectively. In order to eliminate them, based on the statistical hypothesis testing, one must apply a large number of different frequencies. Throughout various numerical test, we observed that if one applied more than $F = 10$ different frequencies, an image with good resolution would appear.

The proposed algorithm could be applied directly to the multiple well-separated thin inclusions with the same thickness h. For that purpose, let us consider the multiple inclusion $\Gamma_{\mathrm{Multi}} = \Gamma_1 \cup \Gamma_2$. MSR matrix $\mathcal{K}$ is collected for $N = 42$ and frequencies $\omega_f \in [\frac{2\pi}{0.3}, \frac{2\pi}{0.2}]$, and corresponding results are shown in Figures 5 and 6. Similarly with the single inclusion cases (see Figures 1 and 2) although MUSIC-type algorithm offers a bad result, the proposed algorithm yields a good result for multiple inclusions case. It is interesting to observe that if an inclusion has a much smaller value of permittivity and/or permeability than the other, it appears to have much smaller magnitude than the other one (see Figure 6).

Now, we end this section with the following example. Throughout some results in [4, 23], it has been observed that MUSIC-type

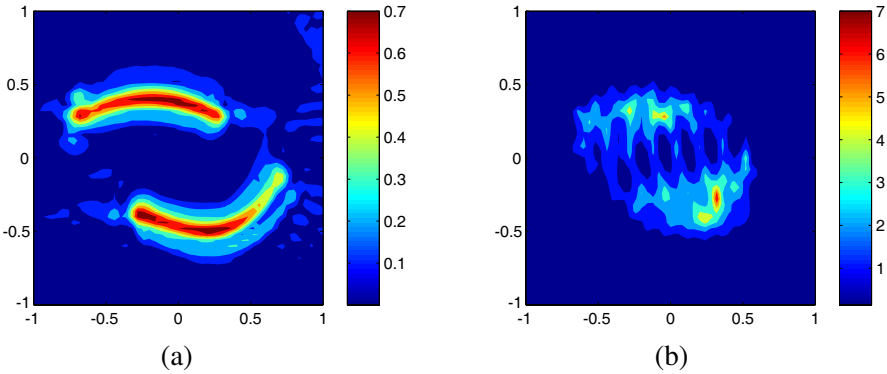

Figure 5. Map of $\mathrm{W}(x)$ and $\mathrm{W}_{\mathrm{MUSIC}}(x)$ for Γ_{Multi} with $\varepsilon_1 = \mu_1 = 5$ and $\varepsilon_2 = \mu_2 = 5$. (a) Map of $\mathrm{W}(x)$. (b) Map of $\mathrm{W}_{\mathrm{MUSIC}}(x)$ at $\omega = \frac{2\pi}{0.3}$.

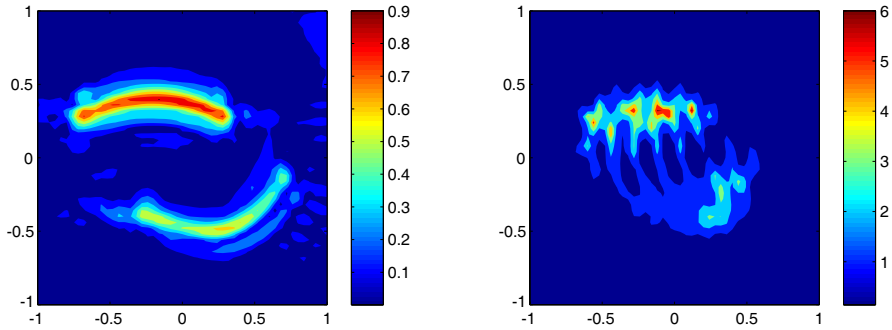

Figure 6. Map of $\mathrm{W}(x)$ and $\mathrm{W}_{\mathrm{MUSIC}}(x)$ for Γ_{Multi} with $\varepsilon_1 = \mu_1 = 10$ and $\varepsilon_2 = \mu_2 = 5$. (a) Map of $\mathrm{W}(x)$. (b) Map of $\mathrm{W}_{\mathrm{MUSIC}}(x)$ at $\omega = \frac{2\pi}{0.3}$.

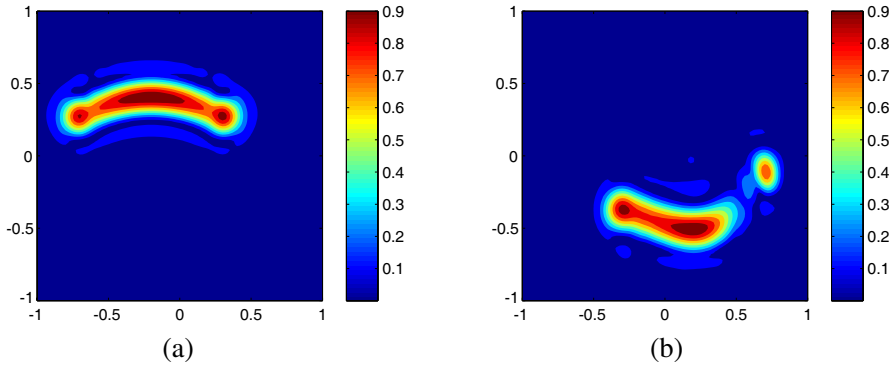

Figure 7. Map of $\mathrm{W}(x)$ for Γ_1 and Γ_2 under the limited range of incident and observation directions. (a) Map of $\mathrm{W}(x)$. (b) Map of $\mathrm{W}(x)$.

algorithm yields poorer results under the limited range of incident and observation directions. However, the proposed imaging algorithm is available for only a limited range of incident and observation directions. For example, let us choose the limited illumination and observation directions $\frac{\pi}{4} \leq \theta_l \leq \frac{3\pi}{4}$. Corresponding result for Γ_1 and Γ_2 appears in Figure 7. By comparing with Figure 1, one can easily observe that a thin inclusion of a simple supporting curve σ_1 is well retrieved. However, compared with Figure 2, poor results appear when the inclusion is of complex shape. It is interesting to observe that the location of the end-points of Γ_2 is well identified, which means that

connected by a straight line, it should be a good initial guess for an iterative solution algorithm.

5. CONCLUSION

A multi-frequency based non-iterative algorithm has been investigated for imaging thin, electromagnetically penetrable curve-like inclusions embedded in a homogeneous space $\mathbb{R}^2$. Results show that this approach works as well for both dielectric and magnetic contrast with respect to the embedding space so that such results of low computational cost could provide initial guesses of the traditional Newton-type based algorithm or of a level-set evolution [1, 15, 26].

In this paper, we consider the imaging in the presence of random noise. The development of a fast and robust imaging algorithm in the presence of random inclusions will be a forthcoming work. Finally, we have been considering a two-dimensional problem. The strategy which is suggested, e.g., mathematical treatment of the asymptotic formula, imaging algorithm, etc., could be extended to the three-dimensional problem.

APPENDIX A. STATISTICAL HYPOTHESIS TESTING

In this appendix, we briefly introduce the statistical hypothesis testing. We suggest [3, 16, 19] for a more detailed description. Let us assume that measured MSR matrix in the presence of single thin inclusion Γ is polluted by Additive White Gaussian Noise (AWGN):

$$\mathcal{K}_{\text{meas}} = \mathcal{K}_{\text{asym}} + \delta\mathcal{W},$$

where the elements of matrix $\mathcal{K}_{\text{asym}}$ is given by (3), $\delta > 0$ being a real number and $\mathcal{W}$ being a complex, circularly symmetric Gaussian random vector

$$\mathcal{W} = \mathcal{W}_{\text{real}} + i\mathcal{W}_{\text{imag}}$$

with $\mathcal{W}_{\text{real}}$ and $\mathcal{W}_{\text{imag}}$ having identically independently distributed entries distributed according to the standard normal distribution.

As in the standard statistical hypothesis testing, we postulate two hypotheses and derive a decision rule for deciding between them based on our imaging function. We denote by $\mathcal{H}_0$ the null hypothesis to be tested against the alternative hypothesis $\mathcal{H}_A$:

- The null hypothesis $\mathcal{H}_0$: there is no inclusion,
- The alternative hypothesis $\mathcal{H}_A$: there is an inclusion.

Let us denote by α the false-alarm rate:

$$\alpha = \mathrm{P}[\text{accept } \mathcal{H}_A | \mathcal{H}_0 \text{ is true}]$$

and by $1-\beta$ the success of the test (probability of detection):

$$1-\beta = \mathrm{P}[\text{accept } \mathcal{H}_A | \mathcal{H}_A \text{ is true}],$$

where $\mathrm{P}[A|B]$ denotes the probability of A under the condition B. Given the data the decision rule for accepting $\mathcal{H}_0$ or not can be derived from the Neyman-Pearson lemma which asserts that for a prescribed false alarm rate α the most powerful test corresponds to accepting $\mathcal{H}_A$ for the likelihood ratio of $\mathcal{H}_A$ to $\mathcal{H}_0$ exceeding a threshold determined by α.

We first consider measurements at a single frequency ω. We choose as the test static function:

$$\mathrm{W}(x) = \sum_{m=1}^{M} |\langle \hat{d}(x;\omega), u_m(\omega)\rangle \langle \hat{d}(x;\omega), \bar{v}_m(\omega)\rangle|.$$

We observe that under the null hypothesis $\mathcal{H}_0$:

$$\mathrm{W}(x) \sim \mathcal{N}(0,\delta),$$

while under the alternative hypothesis $\mathcal{H}_A$:

$$\mathrm{W}(x) \sim \mathcal{N}(\zeta(x),\delta)$$

for

$$\zeta(x) := \sum_{m=1}^{M} |\langle \hat{d}(x;\omega), u_m(\omega)\rangle \langle \hat{d}(x;\omega), \bar{v}_m(\omega)\rangle|,$$

where $\mathcal{N}(\zeta,\delta^2)$ denotes the normal distribution with mean ζ and standard deviation δ. By the Neyman-Pearson lemma, the decision rule of accepting $\mathcal{H}_A$ if and only if $\mathrm{W}(x) > \eta$ maximizes the probability of detection for a given false alarm rate α with the threshold

$$\eta = \delta \Phi^{-1}(1-\alpha),$$

where Φ is the Gauss error function. Moreover, since the imaging function is Gaussian with standard deviation δ under the null hypothesis $\mathcal{H}_0$, this definition of η means that the probability of accepting $\mathcal{H}_A$ given that $\mathcal{H}_0$ is true is α. By virtue of [16, 19], the power of the test is given by

$$1-\beta = 1 - \Phi\left(\frac{\eta - \zeta(x)}{\delta}\right).$$

Let $\mathrm{E}[X]$ and $\mathrm{Var}[X]$ be the expected value and variance of X, respectively, then $1-\beta$ can be expressed in terms of the SNR

$$\mathrm{SNR}(x) = \frac{\mathrm{E}[\mathrm{W}(x)]}{\mathrm{Var}[\mathrm{W}(x)]} = \left(\frac{\zeta(x)}{\delta}\right)^2,$$

as

$$1-\beta = 1-\Phi\left(\Phi^{-1}(1-\alpha)-\frac{\zeta(x)}{\delta}\right) = \Phi\left(\sqrt{\mathrm{SNR}(x)}-\Phi^{-1}(1-\alpha)\right)$$

since $\Phi(x) = 1-\Phi(-x)$. Notice that $\zeta(x)$ and $\mathrm{SNR}(x)$ achieve the maximum at $x = x_m$ so that the detection power $1-\beta$ also achieves the maximum at $x = x_m$ for $m = 1, 2, \ldots M$.

When one chooses the imaging function (9) at multiple frequencies ω_f for $f = 1, 2, \ldots, F$, by a straightforward generalization of the arguments, the detection power $1-\beta_F$ is

$$1-\beta_F = \Phi\left(\sqrt{F\times\mathrm{SNR}(x)}-\Phi^{-1}(1-\alpha)\right) \geq 1-\beta.$$

Therefore, we can deduce that the multiple frequencies enhance the imaging performance via higher SNR.

ACKNOWLEDGMENT

The author would like to thank the anonymous referees for their very helpful comments. This work was supported by the new faculty research program 2010 of Kookmin University in Korea.

REFERENCES

1. Álvarez, D., O. Dorn, N. Irishina, and M. Moscoso, "Crack reconstruction using a level-set strategy," *J. Comput. Phys.*, Vol. 228, 5710–5721, 2009.
2. Ammari, H., *An Introduction to Mathematics of Emerging Biomedical Imaging*, Mathematics and Applications Series, Vol. 62, Springer-Verlag, Berlin, 2008.
3. Ammari, H., J. Garnier, H. Kang, W. K. Park, and K. Sølna, "Imaging schemes for perfectly conducting cracks," submitted.
4. Ammari, H., E. Iakovleva, and D. Lesselier, "A MUSIC algorithm for locating small inclusions buried in a half-space from the scattering amplitude at a fixed frequency," *SIAM Multiscale Modeling Simulation*, Vol. 3, 597–628, 2005.
5. Ammari, H. and H. Kang, *Reconstruction of Small Inhomogeneities from Boundary Measurements*, Lecture Notes in Mathematics, Vol. 1846, Springer-Verlag, Berlin, 2004.
6. Beretta, E. and E. Francini, "Asymptotic formulas for perturbations of the electromagnetic fields in the presence of thin imperfections," *Contemp. Math.*, Vol. 333, 49–63, 2003.

7. Capdeboscq, Y. and M. Vogelius, "Imagerie électromagnétique de petites inhomogénéités," *ESAIM: Proc.*, Vol. 22, 40–51, 2008.
8. Chen, X.-D., "Subspace-based optimization method in electric impedance tomography," *Journal of Electromagnetic Waves and Applications*, Vol. 23, No. 11–12, 1397–1406, 2009.
9. Cheney, M., "The linear sampling method and the MUSIC algorithm," *Inverse Problems*, Vol. 17, 591–595, 2001.
10. Cheng, X., B.-I. Wu, H. Chen, and J. A. Kong, "Imaging of objects through lossy layer with defects," *Progress In Electromagnetics Research*, Vol. 84, 11–26, 2008.
11. Chien, W., "Inverse scattering of an un-uniform conductivity scatterer buried in a three-layer structure," *Progress In Electromagnetics Research*, Vol. 82, 1–18, 2008.
12. Conceicao, R. C., M. O'Halloran, M. Glavin, and E. Jones, "Comparison of planar and circular antenna configurations for breast cancer detection using microwave imaging," *Progress In Electromagnetics Research*, Vol. 99, 1–20, 2009.
13. Davy M., J.-G. Minonzio, J. de Rosny, C. Prada, and M. Fink, "Influence of noise on subwavelength imaging of two close scatterers using time reversal method: Theory and experiments," *Progress In Electromagnetics Research*, Vol. 98, 333–358, 2009.
14. Delbary, F., K. Erhard, R. Kress, R. Potthast, and J. Schulz, "Inverse electromagnetic scattering in a two-layered medium with an application to mine detection," *Inverse Problems*, Vol. 24, 015002, 2008.
15. Dorn, O. and D. Lesselier, "Level set methods for inverse scattering," *Inverse Problems*, Vol. 22, R67–R131, 2006.
16. Fannjiang, A. and K. Sølna, "Broadband resolution analysis for imaging with measurement noise," *J. Opt. Soc. Am. A*, Vol. 24, 1623–1632, 2007.
17. Hou, S., K. Huang, K. Sølna, and H. Zhao, "A phase and space coherent direct imaging method," *J. Acoust. Soc. Am.*, Vol. 125, No. 1, 227–238, 2009.
18. Hou, S., K. Sølna, and H. Zhao, "A direct imaging algorithm for extended targets," *Inverse Problems*, Vol. 22, 1151–1178, 2006.
19. Kay, S. M., *Fundamentals of Statistical Signal Processing*, Detection Theory, Prentice Hall, 1998.
20. Lesselier, D. and B. Duchene, "Buried, 2-D penetrable objects illuminated by line sources: FFT-based iterative computations of the anomalous field," *Progress In Electromagnetics Research*, Vol. 5, 351–389, 1991.

21. Li, F., X. Chen, and K. Huang, "Microwave imaging a buried object by the GA and using the S_{11} parameter," *Progress In Electromagnetics Research*, Vol. 85, 289–302, 2008.
22. Nazarchuk, Z. T. and K. Kobayashi, "Mathematical modelling of electromagnetic scattering from a thin penetrable target," *Progress In Electromagnetics Research*, Vol. 55, 95–116, 2005.
23. Park, W. K., "On the imaging of thin dielectric inclusions buried within a half-space," *Inverse Problems*, Vol. 26, 074008, 2010.
24. Park, W. K. and D. Lesselier, "Electromagnetic MUSIC-type imaging of perfectly conducting, arc-like cracks at single frequency," *J. Comput. Phys.*, Vol. 228, 8093–8111, 2009.
25. Park, W. K. and D. Lesselier, "MUSIC-type imaging of a thin penetrable inclusion from its far-field multi-static response matrix," *Inverse Problems*, Vol. 25, 075002, 2009.
26. Park, W. K. and D. Lesselier, "Reconstruction of thin electromagnetic inclusions by a level set method," *Inverse Problems*, Vol. 25, 085010, 2009.
27. Raza, M. I. and R. E. DuBroff, "Detecting dissimilarities in EM constitutive parameters using differential imaging operator on reconstructed wavefield," *Progress In Electromagnetics Research*, Vol. 98, 267–282, 2009.
28. Semnani, A. and M. Kamyab, "Truncated cosine Fourier series expansion method for solving 2-D inverse scattering problems," *Progress In Electromagnetics Research*, Vol. 81, 73–97, 2008.
29. Solimene, R., A. Brancaccio, R. Pierri, and F. Soldovieri, "TWI experimental results by a linear inverse scattering approach," *Progress In Electromagnetics Research*, Vol. 91, 259–272, 2009.
30. Zhou, H., T. Takenaka, J. Johnson, and T. Tanaka, "A breast imaging model using microwaves and a time domain three dimensional reconstruction method," *Progress In Electromagnetics Research*, Vol. 93, 57–70, 2009.